Article

Microstructure and Phase Formation of Novel Al$_{80}$Mg$_5$Sn$_5$Zn$_5$X$_5$ Light-Weight Complex Concentrated Aluminum Alloys

Jon Mikel Sanchez [1,*], Alejandro Pascual [2], Iban Vicario [1], Joseba Albizuri [3], Teresa Guraya [4] and Haize Galarraga [1]

1   Department of Foundry and Steelmaking, TECNALIA, Basque Research and Technology Alliance (BRTA), 48160 Derio, Spain; iban.vicario@tecnalia.com (I.V.); haize.galarraga@tecnalia.com (H.G.)
2   Aeronautics Advanced Manufacturing Center, CFAA, University of the Basque Country, 48170 Zamudio, Spain; alejandro.pascual@ehu.eus
3   Department of Mechanical Engineering, Faculty of Engineering of Bilbao, University of the Basque Country, 48013 Bilbao, Spain; joseba.albizuri@ehu.es
4   Department of Mining & Metallurgical Engineering and Materials Science, Faculty of Engineering of Bilbao, University of the Basque Country, 48013 Bilbao, Spain; teresa.guraya@ehu.eus
*   Correspondence: jonmikel.sanchez@tecnalia.com

Abstract: In this work, three novel complex concentrated aluminum alloys were developed. To investigate the unexplored region of the multicomponent phase diagrams, thermo-physical parameters and the CALPHAD method were used to understand the phase formation of the Al$_{80}$Mg$_5$Sn$_5$Zn$_5$Ni$_5$, Al$_{80}$Mg$_5$Sn$_5$Zn$_5$Mn$_5$, and Al$_{80}$Mg$_5$Sn$_5$Zn$_5$Ti$_5$ alloys. The ingots of the alloys were manufactured by a gravity permanent mold casting process, avoiding the use of expensive, dangerous, or scarce alloying elements. The microstructural evolution as a function of the variable element (Ni, Mn, or Ti) was studied by means of different microstructural characterization techniques. The hardness and compressive strength of the as-cast alloys at room temperature were studied and correlated with the previously characterized microstructures. All the alloys showed multiphase microstructures with major α-Al dendritic matrix reinforced with secondary phases. In terms of mechanical properties, the developed alloys exhibited a high compression yield strength up to 420 MPa, high compression fracture strength up to 563 MPa, and elongation greater than 12%.

Keywords: complex-concentrated alloys; aluminum alloys; high-entropy alloys; theoretical modeling; CALPHAD; mechanical properties; lightweight alloys; casting

1. Introduction

A great deal of effort has been devoted to the development of new lightweight materials during the last decades. Al-based alloys have received considerable attention, especially in the automotive and aerospace industries, due to the possibility of their light weight and consequent reduction of greenhouse gas emissions. Commercial Al alloys consist of Al as base element and small quantities of solute elements added to improve the mechanical and physical properties. In some cases, these restricted compositions lead to some limitations, such as their performance at high temperatures or low wear resistance.

One research focus with relevance to light weight in the transport industry includes the so-called high entropy alloys (HEAs) [1,2]. HEAs were defined as alloys of five or more metallic elements in equimolar or near-equimolar concentrations between 5 and 35 at.%. The main goal of this approach was to stabilize a single-phase solid solution (SS) by reducing Gibbs free energy to obtain simple crystal structures instead of brittle intermetallic compounds (IC). HEAs have received significant attention since initial reports in 2004 [3,4]. These alloys exhibit excellent mechanical properties, corrosion-oxidation resistance, and wear behavior [5–9], having numerous engineering applications [10].

Most of the HEAs are composed of transition metal elements, with densities like steels. To predict SS phase formation in HEAs, various empirical approaches based on Hume-Rothery rules and thermodynamic parameters were proposed [11,12]. These parameters commonly include the enthalpy of mixing in the liquid phase (ΔH_{mix}), atomic size difference (δ_r), Pauling electronegativity difference ($\Delta\chi$) and the Ω-parameter. These parameters are not sufficient conditions to form single-phase SS [13], but can be used as preliminary designing guide to define an alloy system.

Concerning HEAs composed of low-density elements, known as lightweight-HEAs (LW-HEAs), a great effort has been done to obtain alloys with densities like those of light structural materials such as Al or Ti alloys. Despite the initial concept of maximizing the configurational entropy to obtain single-phase SS in HEAs, to date only $Al_{20}Li_{20}Mg_{10}Sc_{20}Ti_{30}$ LW-HEA [14] avoided the formation of brittle IC displaying single-phase SS microstructure [15–20]. Hence, more restrictive values than previously proposed for HEAs for the stabilization of disordered SS were proposed for alloys containing low density elements [17]: $-1 \text{ kJ/mol} \leq \Delta H_{mix} \leq 5 \text{ kJ/mol}$, $\delta_r < 4.5\%$, $\Omega > {\sim}10$ and $\Delta\chi \leq 0.175$. Thereby, LWHEAs can be regarded as hard, brittle and strong multiphase materials due to large solution and/or precipitation hardening. These alloys are often called lightweight complex concentrated alloys (CCAs), low-density multi-principal elements alloys, entropic alloys, medium entropy aluminum alloys, etc. [17,21–26] and are inspired by the high entropy concept, but expanding the compositional definition given at the beginning of HEAs.

Yang et al. studied multi-principal component alloys containing high concentrations of Al, Mg, Li, Zn, Cu and/or Sn, all the studied alloys exhibited high compressive strength [17]. The compressive plastic strain of $Al_{80}Li_5Mg_5Zn_5Sn_5$ and $Al_{80}Li_5Mg_5Zn_5Cu_5$ alloys reached up to 17%. Instead, AlLiMgZnSn and $AlLi_{0.5}MgZn_{0.5}Sn_{0.2}$ alloys exhibited brittle behavior, with plastic strain values below 1.2%. Deviating from the definition of HEAs, the compressive ductility of Al-Li-Mg-Ca-Si near-equiatomic alloys was improved by adjusting the composition, a ductility of 60% and 45% were reported in $Al_{15}Li_{39}Mg_{45}Ca_{0.5}Si_{0.5}$ and $Al_{15}Li_{35}Mg_{48}Ca_1Si_1$ alloys respectively [21]. Following the route to design non-equiatomic medium entropy alloys [27], the $Al_{65}Cu_5Mg_5Si_{15}Zn_5X_5$ and $Al_{70}Cu_5Mg_5Si_{10}Zn_5Y_5$ (X = Fe, Ni and Y = Cr, Mn, Zr, in at.%) alloys exhibited moderate plastic deformation and high compressive strength up to 644 MPa, and microhardness value up to 264 HV [22]. Recently, Mitrica et al. studied several alloys in the Al-Cu-Si-Zn-Mg and Al-Mn-Zn-Mg-Si systems, where the $Al_{3.4}Cu_{0.5}Si_{0.2}Zn_{0.5}Mg_{0.2}$ and $Al_3Mn_{0.2}Zn_{0.3}Mg_{0.7}Si_{0.8}$ alloys exhibited the highest strength and hardness in each system [26].

There is still a vast unknown space in low density multicomponent phase diagrams that remains unexplored, from the corners of well-known traditional Al alloys (~90 wt.% of the base element) to the center of the equimolar LW-HEAs. Therefore, in this research, the unexplored region of the multicomponent phase diagrams has been considered. The main objective of this research is to develop three novel $Al_{80}Mg_5Sn_5Zn_5Ni_5$, $Al_{80}Mg_5Sn_5Zn_5Mn_5$ and $Al_{80}Mg_5Sn_5Zn_5Ti_5$ CCAs. As it is well-known, the highest strengths and highest application temperatures are met by alloys with a controlled distribution of a secondary phases [28]. Thus, the alloys were developed to obtain a major SS phase reinforced with different IC, with a density below 3.3 g/cm^3. Experimental densities are nearly 20% higher density than currently available commercial aluminum alloys, and nearly 35% lighter than titanium alloys. The ingots of the alloys were manufactured by a gravity permanent mold casting process, and the use of expensive, dangerous, or scarce elements was avoided. Then, the microstructures, hardness, and compressive strength of the as-cast alloys at room temperature (RT) were studied to evaluate the suitability of the developed CCAs.

2. Materials and Methods

The software Thermo-Calc (v. 2020b, Thermo-Calc Software AB, Stockholm, Sweden) [29] in conjunction with the TCAL7 thermodynamic database was used for calculation of the equilibrium phases as a function of temperature.

Experimental alloys were prepared in an induction furnace VIP-I (Inductotherm Corp., Rancocas, NJ, USA) in an alumina crucible using 99.95% pure Al, Mg, Sn and Zn. Tablets of Al-Ni, Al-Mn and Al-Ti containing 75 wt.% of Ni, 80 wt.% of Mn, and 75 wt.% of Ti respectively were used. Firstly, Al was melted to guarantee a bath base where Mn, Ni or Ti was subsequently dissolved. Finally, Sn, Mg, and Zn were added to the molten alloy and held between 776 and 795 °C for 10 min to reach complete dissolution. Finally, the melt was cooled down to 700 °C and poured manually into a preheated steel mold at 200 °C.

Ingots of 200 mm × 80 mm × 40 mm were obtained for each alloy. The microstructural samples were cut from the ingots and prepared according to standard metallographic procedures, by hot mounting in conductive resin, grinding, and polishing. The X-ray diffraction (XRD) equipment used to characterize the crystal structures of the alloys was a D8 ADVANCE (BRUKER, Karlsruhe, Germany) diffractometer, with Cu Kα radiation, operated at 40 kV and 30 mA. The diffraction diagrams were measured at the diffraction angle 2θ, range from 10° to 90° with a step size of 0.01°, and 1.8 s/step. The powder diffraction file (PDF) database 2008 was applied for phase identification. The microstructure, the different regions, and the averaged overall chemical composition of each sample were investigated by an optic microscope model DMI5000 M (LEICA Microsystems, Wetzlar, Germany) and a scanning electron microscope (SEM), equipped with an energy dispersive X-ray spectrometry (EDS) model JSM-5910LV (JEOL, Croissy-sur-Seine, France).

A Vickers hardness FV-700 model (FUTURE-TECH, Kawasaki, Japan) measurer was employed on the polished sample surface using a 1 kg load, applied for 10 s. At least 10 random individual measurements were made for each test. Cylindrical specimens for compression testing were machined from the ingots, with a diameter of 13 mm and a height of 26 mm, giving an aspect ratio of 1:2. Compression testing was performed using a MTS Insight 100 kN Extended Length (MTS Systems Corporation, Eden Prairie, MN, USA) at RT with a strain rate of 0.001 s^{-1}. For the accurate measurement of Young's modulus, a clip-on extensometer mounted on the specimens were used. At least five specimens were recorded to ensure repeatability. Finally, density measurement was conducted using the Archimedes method.

3. Results and Discussion

3.1. Thermo-Physical Parameters for Phase Formation in HEAs

In this work, the unexplored Al-Mg-Sn-Zn-X system (X = Ni, Mn and Ti) was selected to study the thermo-physical parameters proposed for phase formation in HEAs. The mixing enthalpy (ΔH_{mix}) is expressed as:

$$\Delta H_{mix} = 4 \sum\nolimits_{i=1,\ i \neq j}^{n} C_i C_j \, \Delta H_{i-j}^{mix} \tag{1}$$

where n is the number of the elements in the alloy, C_i is the atomic ratio of the ith element; C_j is the atomic ratio of the jth element, and ΔH_{i-j}^{mix} is the enthalpy of mixing between ith and jth elements calculate by Miedema's model [30]. The atomic size difference (δ) is obtained by:

$$\delta = 100 \sqrt{\sum\nolimits_{i=1}^{n} C_i \left(1 - \frac{r_i}{\bar{r}}\right)^2} \tag{2}$$

where r_i is the atomic radius of ith element and $\bar{r}$ is the composition weighted average atomic radius. The Pauling electronegativity difference is calculated as:

$$\Delta \chi = \sqrt{\sum\nolimits_{i=1}^{n} C_i \left(\chi_i - \bar{\chi}\right)^2} \tag{3}$$

where χ_i is the Pauling electronegativity for the ith component and $\bar{\chi}$ is the composition weighted average electronegativity of all the components. The Ω parameter, which can be regarded as the ratio between the enthalpy and the entropy in the liquid state, is given by:

$$\Omega = \frac{\overline{T_m}\Delta S_{mix}}{|\Delta H_{mix}|} \tag{4}$$

where $\Delta S_{mix} = \Delta S_{conf} = -R\sum_i^n C_i \ln C_J$, T_m is the composition-weighted average melting point of the alloy and R is the gas constant (8.314 J·mol^{-1}·K^{-1}). Subsequently, the theoretical density (ρ_t) of the targeted alloys was calculated by using the assumptions of a rule of mixture:

$$\rho_t = \frac{\sum C_i A_i}{\sum \frac{C_i A_i}{\rho_i}} \tag{5}$$

where A_i is the atomic weight of the ith element; ρ_i is the density of the ith element. In the preliminary study of the thermo-physical parameters for phase formation in HEAs, three different alloy systems were considered. The first system is based on the nominally AlMgSnZnX equimolar composition. The second $Al_{35}Mg_{35}Sn_5Zn_{20}X_5$ system is based on the compositional definition of HEAs given by Yeh et al. [4], and optimized to obtain the lowest possible density. Finally, the $Al_{80}Mg_5Sn_5Zn_5X_5$ system was studied, with Al as the main element, and the quantity of the other elements was kept over 5 at.% to be considered as principal element [31]. Hence, a multi-principal element alloys composed of five elements were studied with a composition of the main element of 80 at.%, which is the upper limit for an alloy consisting of five multi-principal elements. In Table 1, the calculated parameters of the defined systems are summarized.

Table 1. Calculated thermo-physical parameters and the theoretical density for the developed alloys and their equiatomic and near equiatomic counterparts.

Alloy	ΔH_{mix} (kJ/mol)	δ (%)	$\Delta\chi$	Ω	ρ_t (g/cm^3)
AlMgSnZnNi	−7.7	8.6	0.234	1.7	5.20
$Al_{35}Mg_{35}Sn_5Zn_{20}Ni_5$	−4.3	6.9	0.196	2.3	3.49
$Al_{80}Mg_5Sn_5Zn_5Ni_5$	−3.3	4.3	0.122	1.8	3.37
AlMgSnZnMn	−4.9	8.3	0.209	2.5	5.12
$Al_{35}Mg_{35}Sn_5Zn_{20}Mn_5$	−3.1	6.8	0.177	3.3	3.48
$Al_{80}Mg_5Sn_5Zn_5Mn_5$	−2.7	4.2	0.104	2.2	3.36
AlMgSnZnTi	−5.8	5.2	0.209	2.3	4.68
$Al_{35}Mg_{35}Sn_5Zn_{20}Ti_5$	−3.7	5.9	0.177	2.8	3.40
$Al_{80}Mg_5Sn_5Zn_5Ti_5$	−4.4	3.2	0.105	1.4	3.27

As can be observed, the very restrictive values of ΔH_{mix} between −1 and 5 kJ/mole to avoid the formation of ICs in LW-HEAs are very difficult to satisfy, especially in equiatomic alloys. In all the alloying systems, the highest negative value of ΔH_{mix} belongs to equiatomic compositions, followed by the $Al_{35}Mg_{35}Sn_5Zn_{20}X_5$ system, and finally, by the $Al_{80}Mg_5Sn_5Zn_5X_5$ system. Therefore, the values of the ΔH_{mix} of the $Al_{80}Mg_5Sn_5Zn_5X_5$ system are closer to satisfying it than their equiatomic counterparts. Following the proposed criteria of δ_r below 4.5% and $\Delta\chi$ equal or below 0.175 to form SS, only $Al_{80}Mg_5Sn_5Zn_5X_5$ system satisfy these criteria. On the other hand, all the calculated values of Ω are very far away of those proposed for the formation of SS in LW-HEAs. The ΔH_{mix} must be near zero and ΔS_{mix} as high as possible to satisfy this requirement, and there are few combinations of low-density elements that satisfy it. Finally, the calculated ρ_t of the $Al_{80}Mg_5Sn_5Zn_5X_5$ system also shows the benefit of this system over the other systems.

From the preliminary study of the thermo-physical parameters for phase formation in HEAs, the $Al_{80}Mg_5Sn_5Zn_5X_5$ system was selected. In this system, a microstructure predominantly formed by α-Al phase with other/s ICs is expected to be stabilized. Considering that it is very difficult to keep the ΔH_{mix} values within the limits of SS formation, a system as close as possible to the critical values has been selected, as it is impossible to avoid the formation of ICs attempting to control their volume.

3.2. Equilibrium Phase Diagram of the Alloys

Equilibrium phase diagrams of the developed alloys are shown in Figure 1. All the alloys are expected to be composed of a mixture of five different phases at equilibrium. Hence, the alloys are expected to be composed of at least of FCC (A1), Mg_2Si (C1) and Laves (C14) phases, also known as α-Al, Mg_2Sn, and η-$MgZn_2$ phases, respectively. The Mg_2Sn is a desirable phase to improve the mechanical properties by grain refinement and precipitation strengthening in Mg-based alloys [32,33]. The η-$MgZn_2$ is typical phase in Al-Zn-Mg-(Cu) alloys that plays an important role in the excellent mechanical properties of the precipitation hardenable 7xxx series.
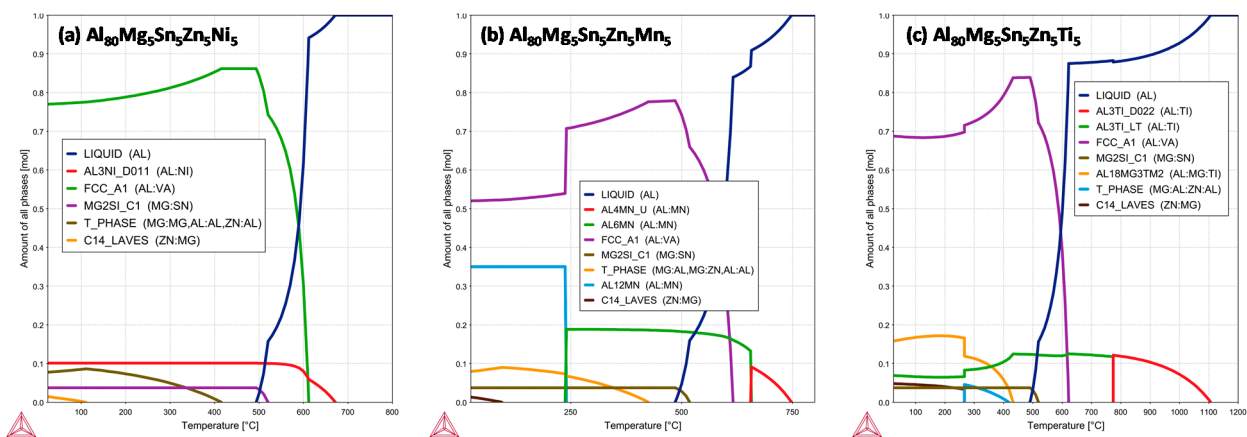

Figure 1. Equilibrium phase diagrams in function of temperature of the selected alloys (**a**) $Al_{80}Mg_5Sn_5Zn_5Ni_5$; (**b**) $Al_{80}Mg_5Sn_5Zn_5Mn_5$ and (**c**) $Al_{80}Mg_5Sn_5Zn_5Ti_5$.

$Al_{80}Mg_5Sn_5Zn_5Ni_5$ alloy (Figure 1a) was expected to be mainly composed of FCC phase (α-Al), 77 mol % at RT. The major reinforce phase is Al_3Ni ($D0_{11}$), which precipitates at 672 °C, and its amount of phase (10 mol %) remains stable below 557 °C. At 521 °C the Mg_2Si (Mg_2Sn) compound precipitates from liquidus, the amount of this phase is 4 mol % at RT. The T-phase defined by Thermo-Calc, compositionally $(Al,Zn)_{49}Mg_{32}$, precipitates from FCC matrix at 413 °C. The amount of this phase is 8 mol % at RT. Recently, the benefits of this phase in Al-Zn-Mg-Cu alloy strengthened by T-phase were reported [34]. Finally, the η-$MgZn_2$ phase precipitates from T-$(Al,Zn)_{49}Mg_{32}$ at 112 °C, and the amount of this phase is below 1 mol %.

The $Al_{80}Mg_5Sn_5Zn_5Mn_5$ alloy equilibrium phase diagram (Figure 1b), was distinctively different from a previously studied alloy containing Ni. Both alloys were expected to be composed of major α-Al matrix reinforced by T-$(Al,Zn)_{49}Mg_{32}$; Mg_2Sn and $MgZn_2$ minor phases, but there is a quantitative and qualitative transformation below 238 °C. At this temperature, the amount of phase of α-Al decreased drastically from 83 mol % to 52 mol % due to the precipitation of $Al_{12}Mn$ from the supersaturated α-Al phase. The amount of $Al_{12}Mn$ phase is 34 mol % at RT. The minor phases show a similar precipitation pattern than alloy containing Ni.

The phase diagram of $Al_{80}Mg_5Sn_5Zn_5Ti_5$ alloy (Figure 1c), showed that the liquidus temperature is noticeably higher than previously studied alloys due to the formation of Al_3Ti ($D0_{22}$) intermetallic phase at 1108 °C. This phase changes to Al_3Ti (LT) at 760 °C and represent the 7 mol % at equilibrium. The remaining phases at RT are the ternary $Al_{18}Mg_3Ti_2$ (17 mol %), and the previously defined Mg_2Sn (4 mol %) and $MgZn_2$ (5 mol %). In this case, T-phase precipitates at 416 °C and dissolve at 265 °C in $Al_{18}Mg_3Ti_2$ phase.

3.3. Microstructural Characterization

The overall composition of the alloys was estimated using EDS over large areas. The average values of at least three random measurements are presented in Table 2. The

overall values of all alloys deviate slightly from the target compositions. At least one other residual components element was measured by EDS in each alloy. There is little difference between the target and experimental alloy composition, because some elemental vaporization and/or oxidation may have occurred during melting.

Table 2. Elemental composition in at.% of the manufactured alloys obtained by EDS.

Alloy	Al	Mg	Sn	Zn	Ni	Mn	Ti	Other/s
$Al_{80}Mg_5Sn_5Zn_5Ni_5$	77	3	5	7	5	-	-	~2
$Al_{80}Mg_5Sn_5Zn_5Mn_5$	76	4	6	8	-	4	-	~2
$Al_{80}Mg_5Sn_5Zn_5Ti_5$	75	4	6	8	-	-	5	~2

Figure 2a,b show the SEM micrograph of as-cast $Al_{80}Mg_5Sn_5Zn_5Ni_5$ alloy at low and high magnification respectively. In Figure 2a, a coarse dendritic structure is observed, where the matrix has a black contrast and the interdendritic space has the brightest contrast. A platelet-like region with grey contrast is also distinguished in the same figure. In Figure 2b, the dendritic matrix was labelled as D and the platelet like morphology as IC. In the interdendritic space, two different regions are distinguished, a white contrast region (ID1) and a grey contrast region (ID2).
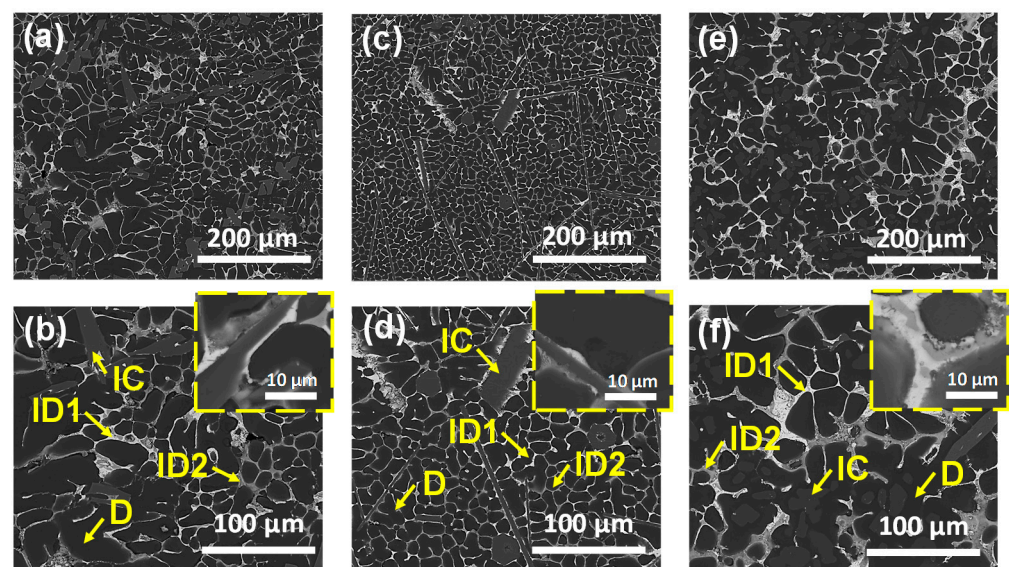

Figure 2. SEM images of (**a**) low and (**b**) high magnification of $Al_{80}Mg_5Sn_5Zn_5Ni_5$, (**c**) low and (**d**) high magnification of $Al_{80}Mg_5Sn_5Zn_5Mn_5$; (**e**) low and (**f**) high magnification of $Al_{80}Mg_5Sn_5Zn_5Ti_5$.

Figure 2c,d show the SEM micrograph of as-cast $Al_{80}Mg_5Sn_5Zn_5Mn_5$ alloy at low and high magnification respectively. It is evident that the substitution of Ni by Mn lead to a significant microstructural alteration. Thereby, in Figure 2c, the microstructure shows fine net-like globular dendrites, even though the interdendritic space also displays the brightest contrast. In this case, spherical, rhomboidal, and plate-like morphologies with the same contrast are distinguished. These different morphologies were identified as Al_6Mn phase independent of the particle morphology [35], and attributed to different dislocation substructures in dependence on the matrix orientation. In Figure 2d, the dendritic matrix was labelled as D, the spherical, rhomboidal, and plate-like morphologies as IC. In this alloy, the interdendritic space also was composed of a white contrast region (ID1) and a grey contrast region (ID2).

Figure 2e,f show the SEM micrograph of as-cast $Al_{80}Mg_5Sn_5Zn_5Ti_5$ alloy at low and high magnification respectively. In Figure 2e, the dendrites with a black contrast show pillar-like morphology, and two regions are distinguished in the interdendritic space at

low magnification. Finally, a rounded region inside the dendrites with a gray contrast is also distinguished in the same figure. In Figure 2f, the dendrites are labelled as D, and the interdendritic space was composed of a major white contrast region (ID1) and a minor grey contrast region (ID2).

Figure 3 shows the SEM + EDS micrograph and the elemental mapping of as-cast $Al_{80}Mg_5Sn_5Zn_5Ni_5$ alloy. The major dendritic phase (D) is mainly composed of Al with a small amount of Mg and Zn. The platelet-like particles (IC) are composed of Al and Ni. The bright white region in the interdendritic space (ID1) is composed of Sn and Mg, and the grey contrast region (ID2) is mainly composed of Zn.
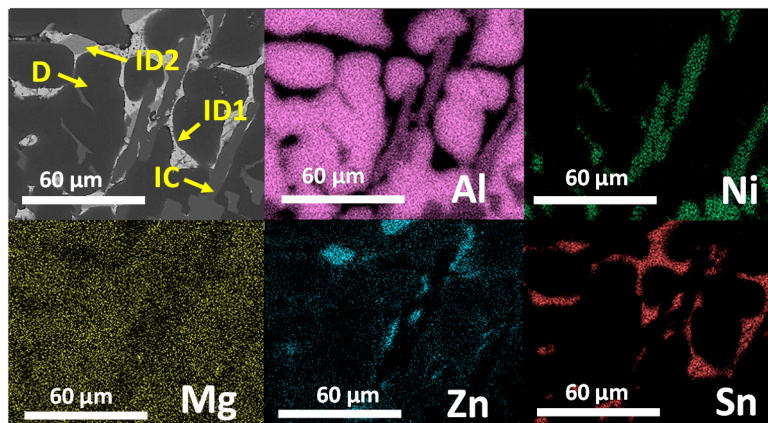
Figure 3. SEM image and EDS elemental mapping of the as-cast $Al_{80}Mg_5Sn_5Zn_5Ni_5$ alloy.

Figure 4 shows the SEM + EDS micrograph and the elemental mapping of $Al_{80}Mg_5Sn_5Zn_5Mn_5$ alloy. The dendritic phase (D) is mainly composed of Al with small amount of Mg and Zn. The major interdendritic region (ID1) is composed of Sn and Mg and the minor region (ID2) of Zn. In this case, the addition of Mn leads to the formation of Al-Mn-rich (IC) different morphologies with similar qualitative elemental composition.
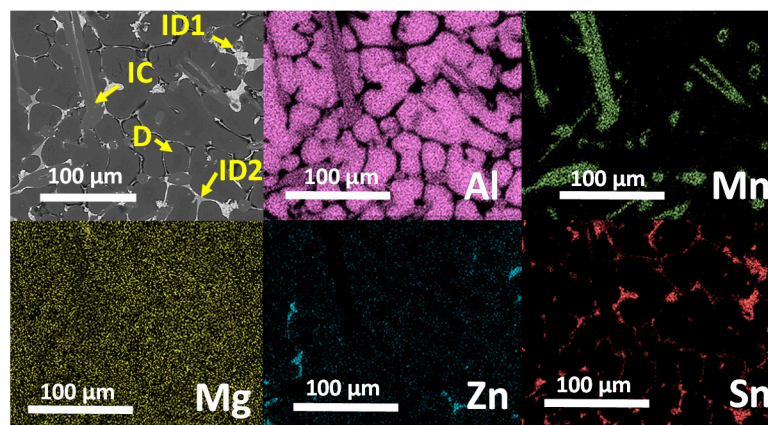

Figure 4. SEM image and EDS elemental mapping of the as-cast $Al_{80}Mg_5Sn_5Zn_5Mn_5$ alloy.

Figure 5 shows the SEM + EDS micrograph and the elemental mapping of as-cast $Al_{80}Mg_5Sn_5Zn_5Ti_5$ alloy. The effect of the addition of Ti in the formation of intermetallic compounds in the microstructure of $Al_{80}Mg_5Sn_5Zn_5Ti_5$ alloy, is greater than that of the alloys containing Ni and Mn. The major effect observed is that the acicular morphologies are not stabilized in this alloy. The EDS elemental mapping shows similar elemental composition of the dendrites. The interdendritic space also shows the segregation in Sn and Mg-rich (ID1) and Zn-rich (ID2) regions. Finally, Ti was precipitated in the dendritic region in combination with Al. This region labelled as IC presents a globular morphology.
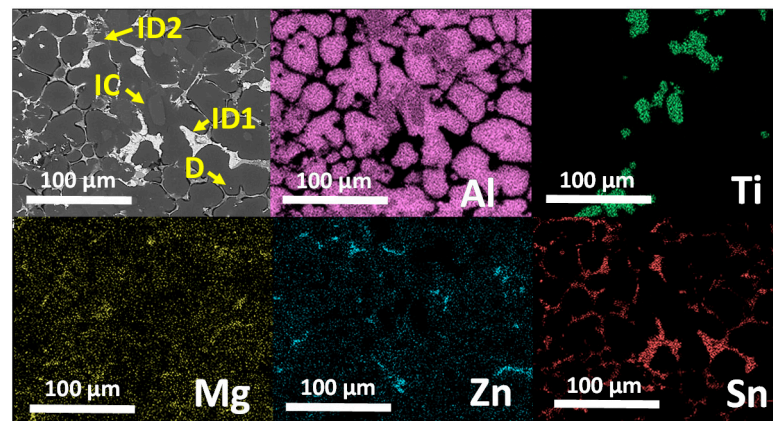
Figure 5. SEM image and EDS elemental mapping of the as-cast Al$_{80}$Mg$_5$Sn$_5$Zn$_5$Ti$_5$ alloy.

Figure 6 shows the XRD patterns of the experimental alloys in the as-cast condition, the Al$_{80}$Mg$_5$Sn$_5$Zn$_5$X$_5$ alloys were confirmed to be multiphase microstructures. According to the XRD data, at least the diffraction patterns of α-Al (cubic, *Fm-3m*), Zn (hexagonal, *P6$_3$/mmc*) and Mg$_2$Sn (cubic, *Fm-3m*) phases were indexed in all the alloys. In the XRD diagram of Al$_{80}$Mg$_5$Sn$_5$Zn$_5$Ni$_5$ alloy, the expected Al$_3$Ni (orthorhombic, *Pnma*) phase also was indexed, which agrees with the result obtained by SEM + EDS. In the XRD diagram of Al$_{80}$Mg$_5$Sn$_5$Zn$_5$Mn$_5$ alloy, the peaks of the orthorhombic Al$_6$Mn phase were found. From equilibrium thermodynamic calculations, a phase transformation from Al$_6$Mn to Al$_{12}$Mn phase was expected at 141 °C, but instead of the cubic Al$_{12}$Mn phase the orthorhombic Al$_6$Mn phase was indexed in the XRD diagram. Thus, the results obtained by XRD patterns are consistent with the thermodynamic equilibrium above 141 °C, which is related to the non-equilibrium solidification of the permanent mold casting process. Finally, in the XRD diagram of Al$_{80}$Mg$_5$Sn$_5$Zn$_5$Ti$_5$ alloy, the predicted Al$_3$Ti (tetragonal, *I39/mmm*) phase also was indexed. The phases indexed in the diagram showed a better agreement with the equilibrium phases predicted above 421 °C instead of the phases at RT. This is consistent with the non-equilibrium solidification of the casting process.
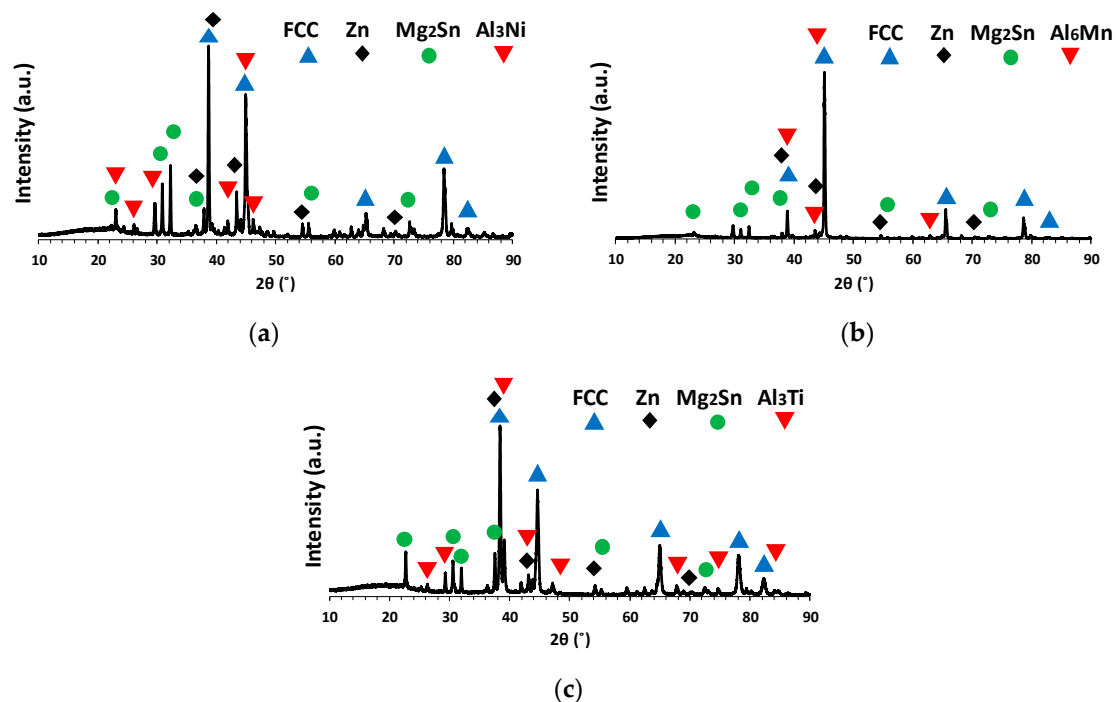

(a)

(b)

(c)

Figure 6. XRD diffraction patterns of the as-cast alloys (**a**) Al$_{80}$Mg$_5$Sn$_5$Zn$_5$Ni$_5$; (**b**) Al$_{80}$Mg$_5$Sn$_5$Zn$_5$Mn$_5$ and (**c**) Al$_{80}$Mg$_5$Sn$_5$Zn$_5$Ti$_5$.

XRD patterns in Figure 6 lead to some discrepancies between CALPHAD predictions and experimental procedures. The Zn phase was not expected to be in thermodynamic equilibrium of the studied systems. However, the different microstructural characterization techniques employed in this paper, including diffraction peaks of Zn phase (hexagonal, $P6_3/mmc$), confirmed the formation of Zn-rich region. Thus, in Figure 7 the semi-quantitative chemical composition of the interdendritic regions defined as ID2 in all the alloys is summarized.
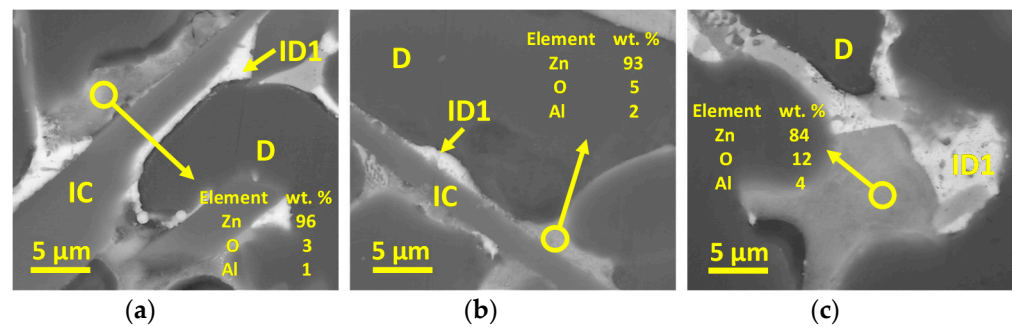

Figure 7. Semi-quantitative chemical composition of ID2 regions obtained by EDS (**a**) $Al_{80}Mg_5Sn_5Zn_5Ni_5$; (**b**) $Al_{80}Mg_5Sn_5Zn_5Mn_5$ and (**c**) $Al_{80}Mg_5Sn_5Zn_5Ti_5$.

As can be seen in Figure 7, ID2 is mainly composed of Zn with a small amount of O and Al. Therefore, the discrepancies between CALPHAD and experimental results may be due to the high melting temperatures reached during the casting process to dissolve Ni, Mn, and Ti. This promoted a partial oxidation of Zn at high temperatures stabilizing Zn-O phase instead of the thermodynamically stable phase (T-phase) predicted by Thermo-Calc.

3.4. Mechanical Properties

To evaluate the mechanical properties of the as-cast alloys, Vickers hardness and compressive test were conducted at RT. The compressive engineering stress-strain curves of the alloys are plotted in Figure 8. The highest strength is obtained by Ti addition, while the alloys containing Ni and Mn showed similar compressive mechanical properties. The curve corresponding to $Al_{80}Mg_5Sn_5Zn_5Ti_5$ alloy (the blue line denoted as c), shows the highest hardening rate.
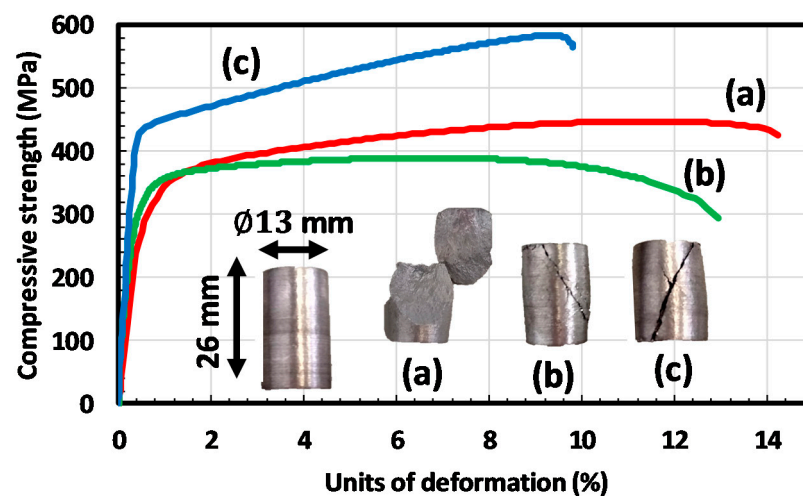

Figure 8. Compressive engineering stress—strain curves of (**a**) $Al_{80}Mg_5Sn_5Zn_5Ni_5$; (**b**) $Al_{80}Mg_5Sn_5Zn_5Mn_5$ and (**c**) $Al_{80}Mg_5Sn_5Zn_5Ti_5$.

In general terms of mechanical properties, the as-cast alloys showed a good balance of mechanical properties, combining high strength and hardness with moderate deformation.

The compressive mechanical properties showed that the $Al_{80}Mg_5Sn_5Zn_5Ti_5$ alloy exhibited the highest strength and hardening rate. This is correlated with the formation of globular Al_3Ti phase, instead the formation of the acicular phases in the alloys containing Ni and Mn. There is also a good correlation between hardness and elongation values in the alloys studied, with a decrease in elongation values when the hardness of the alloy is increased, as is usual in metallic alloys.

The experimental density, hardness, and compressive mechanical properties with the standard deviations of the developed alloys are summarized in Table 3. The calculated densities in Table 1 showed good agreement with the experimental results. The test results revealed that all the alloys exhibited high compressive offset yield strength ($\sigma_{C0.2}$) and ultimate compressive strength (σ_{CU}) exceeding 317 MPa and 368 MPa, respectively. The hardness of the alloys demonstrated high values exceeding those of Al-based alloys, and the $Al_{80}Mg_5Sn_5Zn_5Ti_5$ alloy showed the highest hardness averaging 159 HV.

Table 3. Experimental density, hardness and compressive properties of the developed alloys.

Alloy	ρ (g/cm^3)	HV0.1	E (GPa)	$\sigma_{C0.2}$ (MPa)	σ_{CU} (MPa)	ε (%)
$Al_{80}Mg_5Sn_5Zn_5Ni_5$	3.33	128 ± 12	62 ± 1	317 ± 3	447 ± 32	15 ± 2
$Al_{80}Mg_5Sn_5Zn_5Mn_5$	3.15	130 ± 14	80 ± 3	336 ± 8	368 ± 15	14 ± 3
$Al_{80}Mg_5Sn_5Zn_5Ti_5$	3.28	159 ± 11	98 ± 19	420 ± 57	563 ± 30	12 ± 2

4. Conclusions

In this work, three new lightweight CCAs were successfully developed with a density below 3.33 g/cm^3 and manufactured by a standard permanent mold gravity die casting process. From the equilibrium phase diagrams and thermo-physical parameters for phase formation in HEAs, all the alloys were expected to be composed of a mixture of SS + ICs microstructures. This is consistent with the experimental results, since all the as-cast microstructures are composed at least of a major α-Al SS enriched with Zn and Mg, reinforced with a cubic Mg_2Sn intermetallic phase, and the unexpected hexagonal Zn phase. The discrepancies between CALPHAD and experimental results in the formation of this phase were attributed to partial oxidation of Zn during the manufacturing process. The microstructural evolution as a function of the alloying element revealed that, depending on the variable element, Al_3Ni, Al_6Mn, or Al_3Ti phases were also stabilized.

The variable element also affected the grain size of the alloys, with the finest microstructure being that of Mn-containing alloy, followed by Ni-containing alloy, and finally, Ti-containing alloy. This can be related to the precipitation temperatures of the Al_3Ni, Al_6Mn and Al_3Ti phases. The equilibrium phase diagrams of the alloys revealed that Al_3Ti (precipitates at 1108 °C) is the compound with the highest precipitation temperature. The formation and growth of this phase at high temperatures has not allowed it to act as grain refiner, as is common in commercial aluminum alloys. In contrast, Al_3Ni (precipitates at 672 °C) and Al_6Mn (precipitates at 749 °C), with a precipitation temperature closer to the formation of α-Al matrix (precipitation temperature around 610 °C), are more efficient as grain refiners. This can be clearly seen in the equilibrium phase diagrams. When the α-Al matrix starts the solidification in $Al_{80}Mg_5Sn_5Zn_5Ti_5$ alloy, the phase fraction of Al_3Ti phase reached the maximum volume, so there is an insufficient quantity of Ti in the liquid to promote the nucleation of Al-Ti compounds. On the other hand, when the α-Al matrix starts the precipitation in $Al_{80}Mg_5Sn_5Zn_5Ni_5$ and $Al_{80}Mg_5Sn_5Zn_5Mn_5$ alloys, the amount of phase of Al-Ni and Al-Mn phases are growing. This means that some Ni and Mn remain in the liquid phase, promoting the grain refinement of the alloy.

The alloys containing Ni and Mn showed the formation of acicular phases. On the other hand, the addition of Ti led to the formation of a globular phase. This is reflected in the better mechanical properties of $Al_{80}Mg_5Sn_5Zn_5Ti_5$ alloy over alloys containing Ni and Mn. Instead, all the as-cast alloys showed a good balance of mechanical properties, combining high strength and hardness with a deformation up to 15%.

In future studies, some adjustment must be made in the manufacturing process in order to ensure that the final composition is closer to the nominal one, and the effect of different heat treatments in the mechanical properties at RT and high temperatures should be considered. Based on the obtained results, it could be interesting to study the tribological properties of the developed alloys or related systems.

References

1. Gao, M.C.; Liaw, P.K.; Yeh, J.-W.; Zhang, Y. *High-Entropy Alloys: Fundamentals and Applications*; Springer: Berlin/Heidelberg, Germany, 2016; ISBN 9783319270135.
2. Zhang, Y.; Zuo, T.T.; Tang, Z.; Gao, M.C.; Dahmen, K.A.; Liaw, P.K.; Lu, Z.P. Microstructures and properties of high-entropy alloys. *Prog. Mater. Sci.* **2014**, *61*, 1–93. [CrossRef]
3. Cantor, B.; Chang, I.T.H.; Knight, P.; Vincent, A.J.B. Microstructural development in equiatomic multicomponent alloys. *Mater. Sci. Eng. A* **2004**, *375–377*, 213–218. [CrossRef]
4. Yeh, J.W.; Chen, S.K.; Lin, S.J.; Gan, J.Y.; Chin, T.S.; Shun, T.T.; Tsau, C.H.; Chang, S.Y. Nanostructured high-entropy alloys with multiple principal elements: Novel alloy design concepts and outcomes. *Adv. Eng. Mater.* **2004**, *6*, 299–303. [CrossRef]
5. Ayyagari, A.; Hasannaeimi, V.; Grewal, H.; Arora, H.; Mukherjee, S. Corrosion, Erosion and Wear Behavior of Complex Concentrated Alloys: A Review. *Metals* **2018**, *8*, 603. [CrossRef]
6. Zhang, W.; Liaw, P.K.; Zhang, Y. Science and technology in high-entropy alloys. *Sci. China Mater.* **2018**, *61*, 2–22. [CrossRef]
7. Lyu, Z.; Fan, X.; Lee, C.; Wang, S.Y.; Feng, R.; Liaw, P.K. Fundamental understanding of mechanical behavior of high-entropy alloys at low temperatures: A review. *J. Mater. Res.* **2018**, *33*, 2998–3010. [CrossRef]
8. Gorsse, S.; Miracle, D.B.; Senkov, O.N. Mapping the world of complex concentrated alloys. *Acta Mater.* **2017**, *135*, 177–187. [CrossRef]
9. Miracle, D.B.; Senkov, O.N. A critical review of high entropy alloys and related concepts. *Acta Mater.* **2017**, *122*, 448–511. [CrossRef]
10. Murty, B.S.; Yeh, J.W.; Ranganathan, S.; Bhattacharjee, P.P. Applications and future directions. In *High-Entropy Alloys*; Elsevier: Amsterdam, The Netherlands, 2019; pp. 247–257. ISBN 9780128160671.
11. Zhang, Y.; Zhou, Y.J.; Lin, J.P.; Chen, G.L.; Liaw, P.K. Solid-solution phase formation rules for multi-component alloys. *Adv. Eng. Mater.* **2008**, *10*, 534–538. [CrossRef]
12. Guo, S. Phase selection rules for cast high entropy alloys: An overview. *Mater. Sci. Technol.* **2015**, *31*, 1223–1230. [CrossRef]
13. Gao, M.C.; Zhang, C.; Gao, P.; Zhang, F.; Ouyang, L.Z.; Widom, M.; Hawk, J.A. Thermodynamics of concentrated solid solution alloys. *Curr. Opin. Solid State Mater. Sci.* **2017**, *21*, 238–251. [CrossRef]
14. Sanchez, J.M.; Vicario, I.; Albizuri, J.; Guraya, T.; Koval, N.; Garcia, J. Compound Formation and Microstructure of As-Cast High Entropy Aluminums. *Metals* **2018**, *8*, 167. [CrossRef]
15. Sanchez, J.M.; Vicario, I.; Albizuri, J.; Guraya, T.; Garcia, J.C. Phase prediction, microstructure and high hardness of novel light-weight high entropy alloys. *J. Mater. Res. Technol.* **2018**, *8*, 795–803. [CrossRef]
16. Feng, R.; Gao, M.; Lee, C.; Mathes, M.; Zuo, T.; Chen, S.; Hawk, J.; Zhang, Y.; Liaw, P. Design of Light-Weight High-Entropy Alloys. *Entropy* **2016**, *18*, 333. [CrossRef]
17. Yang, X.; Chen, S.Y.; Cotton, J.D.; Zhang, Y. Phase Stability of Low-Density, Multiprincipal Component Alloys Containing Aluminum, Magnesium, and Lithium. *JOM* **2014**, *66*, 2009–2020. [CrossRef]
18. Sun, W.; Huang, X.; Luo, A.A. Phase formations in low density high entropy alloys. *Calphad* **2017**, *56*, 19–28. [CrossRef]
19. Kumar, A.; Gupta, M. An Insight into Evolution of Light Weight High Entropy Alloys: A Review. *Metals* **2016**, *6*, 199. [CrossRef]
20. Maulik, O.; Kumar, D.; Kumar, S.; Dewangan, S.K.; Kumar, V. Structure and properties of lightweight high entropy alloys: A brief review. *Mater. Res. Express* **2018**, *5*, 052001. [CrossRef]
21. Jia, Y.; Jia, Y.; Wu, S.; Ma, X.; Wang, G. Novel ultralight-weight complex concentrated alloys with high strength. *Materials* **2019**, *12*, 1136. [CrossRef]

22. Sanchez, J.M.; Vicario, I.; Albizuri, J.; Guraya, T.; Acuña, E.M. Design, Microstructure and Mechanical Properties of Cast Medium Entropy Aluminium Alloys. *Sci. Rep.* **2019**, *9*, 6792. [CrossRef]

23. Shao, L.; Zhang, T.; Li, L.; Zhao, Y.; Huang, J.; Liaw, P.K.; Zhang, Y. A Low-Cost Lightweight Entropic Alloy with High Strength. *J. Mater. Eng. Perform.* **2018**, *27*, 6648–6656. [CrossRef]

24. Zhang, B.; Liaw, P.K.; Brechtl, J.; Ren, J.; Guo, X.; Zhang, Y. Effects of Cu and Zn on microstructures and mechanical behavior of the medium-entropy aluminum alloy. *J. Alloys Compd.* **2020**, *820*, 153092. [CrossRef]

25. Liao, Y.C.; Li, T.H.; Tsai, P.H.; Jang, J.S.C.; Hsieh, K.C.; Chen, C.Y.; Huang, J.C.; Wu, H.J.; Lo, Y.C.; Huang, C.W.; et al. Designing novel lightweight, high-strength and high-plasticity Tix(AlCrNb)100-x medium-entropy alloys. *Intermetallics* **2020**, *117*, 106673. [CrossRef]

26. Mitrica, D.; Badea, I.C.; Olaru, M.T.; Serban, B.A.; Vonica, D.; Burada, M.; Geanta, V.; Rotariu, A.N.; Stoiciu, F.; Badilita, V.; et al. Modeling and Experimental Results of Selected Lightweight Complex Concentrated Alloys, before and after Heat Treatment. *Materials* **2020**, *13*, 4330. [CrossRef]

27. Zhou, Y.; Zhou, D.; Jin, X.; Zhang, L.; Du, X.; Li, B. Design of non-equiatomic medium-entropy alloys. *Sci. Rep.* **2018**, *8*, 1236. [CrossRef]

28. Miracle, D.B.; Miller, J.D.; Senkov, O.N.; Woodward, C.; Uchic, M.D.; Tiley, J. Exploration and development of high entropy alloys for structural applications. *Entropy* **2014**, *16*, 494–525. [CrossRef]

29. Andersson, J.O.; Helander, T.; Höglund, L.; Shi, P.; Sundman, B. Thermo-Calc & DICTRA, computational tools for materials science. *Calphad* **2002**, *26*, 273–312. [CrossRef]

30. Takeuchi, A.; Inoue, A. Classification of bulk metallic glasses by atomic size difference, heat of mixing and period of constituent elements and its application to characterization of the main alloying element. *Mater. Trans.* **2005**, *46*, 2817–2829. [CrossRef]

31. Yeh, J.W. Alloy design strategies and future trends in high-entropy alloys. *JOM* **2013**, *65*, 1759–1771. [CrossRef]

32. Wang, P.Y.; Wang, B.Y.; Wang, C.; Wang, J.G.; Ma, C.Y.; Li, J.S.; Zha, M.; Wang, H.Y. Design of multicomponent Mg–Al–Zn–Sn–Bi alloys with refined microstructure and enhanced tensile properties. *Mater. Sci. Eng. A* **2020**, *791*, 139696. [CrossRef]

33. Wu, K.C.; Yeh, J.W.; Chang, S.Y. Refined microstructure and improved mechanical properties of high-ratio extruded AZ91-xSn magnesium alloy. *Mater. Chem. Phys.* **2015**, *162*, 757–763. [CrossRef]

34. Zou, Y.; Wu, X.; Tang, S.; Zhu, Q.; Song, H.; Cao, L. Co-precipitation of T′ and η′ phase in Al-Zn-Mg-Cu alloys. *Mater. Charact.* **2020**, *169*, 110610. [CrossRef]

35. Yang, P.; Engler, O.; Klaar, H.J. Orientation relationship between Al6Mn precipitates and the Al matrix during continuous recrystallization in Al-1.3%Mn. *J. Appl. Crystallogr.* **1999**, *32*, 1105–1118. [CrossRef]